Eur. Phys. J. Plus (2024) 139:311
https://doi.org/10.1140/epjp/s13360-024-05089-z

THE EUROPEAN PHYSICAL JOURNAL PLUS

Regular Article

Electronic and optical properties of tetrapod quantum dots under applied electric and magnetic fields

R. V. H. Hahn[1], F. Mora-Rey[2], R. L. Restrepo[3], A. L. Morales[2], J. Montoya-Sánchez[2], G. Eramo[4], M. G. Barseghyan[5], A. Ed-Dahmouny[6], J. A. Vinasco[7], D. A. Duque[8], C. A. Duque[2,a]

[1] Departamento de Electrónica y Tecnología de Computadores, Facultad de Ciencias, Universidad de Granada, Granada, Spain
[2] Grupo de Materia Condensada-UdeA, Instituto de Física, Facultad de Ciencias Exactas y Naturales, Universidad de Antioquia UdeA, Calle 70 No. 52-21, Medellín, Colombia
[3] Universidad EIA, Envigado C.P 055428, Colombia
[4] Mediterranean Institute of Fundamental Physics-MIFP, Via Appia Nuova, 31, Marino, Rome 00047, Italy
[5] Department of Solid State Physics, Yerevan State University, 1, Al. Manoogian, 0025 Yerevan, Armenia
[6] SIGER Laboratory, Faculty of Sciences and Technology, Sidi Mohamed Ben Abdellah University, 2202 Fez, Morocco
[7] Institución Universitaria-ITM, Calle 73, 76A-354, vía al Volador, 050034 Medellín, Colombia
[8] GICEI, Facultad de Ingeniería, Institución Universitaria Pascual Bravo, 050034 Medellin, Colombia

Received: 18 December 2023 / Accepted: 11 March 2024
© The Author(s) 2024

Abstract In this work, the ground and low-lying excited states in GaAs tetrapod-shaped nanocrystals and in CdTe/CdS core/shell tetrapod-shaped nanocrystals are computed in the case of a finite confinement potential model using the finite element method and the effective mass approximation. For the single material tetrapod, electron energy levels are studied as a function of size parameters and the intensity of externally applied electric and magnetic fields, while for the core/shell tetrapod the electron and hole states are analyzed relative to size parameters of the core and shell thickness. The results show that the energies are strongly influenced by the tip-arm geometry, arm diameter, shell thickness and the intensity of the electric and magnetic fields.

1 Introduction

Colloidal semiconductor nanostructures have versatile physical and chemical properties, which make them suitable candidates for applications in fields ranging from medicine [1, 2] to optoelectronics [3, 4]. Their properties can be tuned via size and shape modifications, chemical composition and ligand choice, among others. Particularly, control over size and morphology has been of paramount importance in materials chemistry over the last few years, which has allowed the development of synthesis protocols for nanoparticles with specific and particular shapes [5–7]. So, branched nanocrystals (NCs) have emerged as strong alternatives for a wide range of applications [8] thanks to their peculiar geometry that confer on them singular optoelectronic and mechanical properties compared to the conventional spherical nanocrystals. Within these branched NCs, tetrapod-shaped nanocrystals, or simply tetrapods (TPs), are easily manufactured and processed structures whose properties can be tuned in various ways, since they can be found either as single material structures [9] or as core/arm or core/shell structures of combined materials [10–13] or even as a substrate for the growth of spherical metal or semiconductor nanoparticles in the tips of the arms [14–16].

NCs conformed by at least two different crystal phases combine several components with different electronic structures in a single entity, and the band engineering at the interface of these semiconductor heterostructures has a significant relevance in the realization of new functional photovoltaic and optoelectronic devices, thanks to the formation of type I and type II heterostructures [17, 18]. While, an enhancement of photoluminescence has been observed in certain type I heterostructures, type II band alignments commonly lead to a quench of light emission. Type II CdTe/CdSe and CdTe/CdS core/shell nanocrystals have been found to be ideal candidates for their application in photovoltaics, as they present a long-range photoinduced charge separation [18, 19]. Specifically, nanocrystal-polymer hybrid solar cells display a promising performance when constructed with CdTe/CdSe TPs [20, 21], which has brought to light the need for a simple and inexpensive synthetic route for type II CdTe/CdSe and CdTe/CdS tetrapod-shaped NCs [22, 23]. These structures consist of a tetrahedral zinc blende (ZB) core and a wurtzite (WZ) shell grown from the core region [19].

Some authors suggest modifying the properties of the TPs through the introduction of anisotropies in the morphology of the arms, such as variations in the length or diameter of at least one of them [24–26]. This type of anisotropy can be directly fixed in the design stage of the nanocrystals [25, 27] or can occur accidentally during the synthesis process [28, 29]. These tetrapod-shaped NCs have shown significant potential for applications in different fields, such as photovoltaics [30–32], photodetectors and sensing [33,

[a] e-mail: carlos.duque1@udea.edu.co (corresponding author)

Published online: 04 April 2024

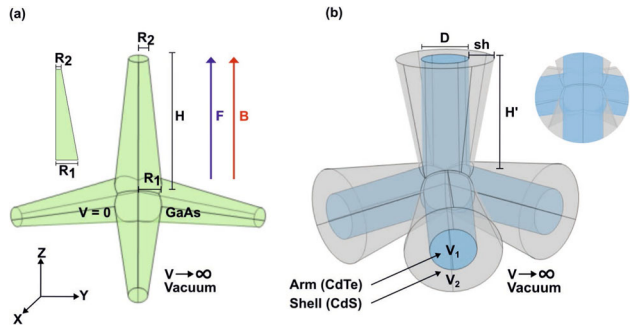

Fig. 1 Schematic representation of the GaAs tetrapod nanostructure **(a)** with fixed lower arm radius, $R_1 = 5$ nm, and variable upper arm radius, R_2 and arm length, H. The CdTe/CdS core/shell tetrapod nanostructure **(b)** is depicted together with a zoom of the geometric center. The arm diameter, D, arm length, H' and shell thickness, sh, are also shown

34], lasing [35] and single-nanoparticle transistors [36]. A judicious choice of band alignment between the materials composing the heterostructured TP can result in a broad delocalization of the electron or hole wave functions from the core into the arms of the tetrapod, which is optimal for applications requiring efficient charge separation, such as in solar cells. Additionally, tetrapod-shaped nanostructures are expected to yield suppressed nonradiative Auger recombination rates thanks to the reduced spatial overlap between the core electron and hole wave functions, turning them to more efficient optical gain material than nanorods or quantum dots [35, 37].

In this work, we try to shed light on the effect of externally applied electric and magnetic fields on tetrapod-shaped nanocrystals made of a single material or in a core/shell configuration. A profound theoretical knowledge of this kind of nanostructures is crucial to their practical implementation, in this article we examine the ground and low-lying excited states for electrons and holes in a GaAs tetrapod-shaped nanocrystal and in a CdTe/CdS core/shell tetrapod-shaped nanocrystal subjected to an electric in/or magnetic field. The influence of size parameters, shell thickness, and the intensity of the electric and magnetic fields on the energy levels of the first electron and hole states will be numerically calculated by solving the stationary Schrödinger equation by means of a finite element method (FEM) within the effective mass approximation. This paper is structured in the following way: in Sect. 2 we present the theoretical model and describe the basic theory, in Sect. 3 we present and discuss our numerical results and, finally, our conclusions are shown in Sect. 4.

2 Theoretical model

In this study, we focus on the energy states and their associated wave functions in two different tetrapod structures, i.e., a GaAs tetrapod and a CdTe/CdS core/shell tetrapod under the influence of external electric and/or magnetic fields, applied along the $z-$direction. Figure 1 presents a schematic representation of the geometry of the two systems considered in this work, together with the main dimensions of the structures and the values of the confinement potential in each region. For the sake of clarity, the reference system is also depicted. For the calculations, the origin of the reference system is set at the geometric center of the tetrapods.

The confining potential profile considered for the CdTe/CdS core/shell TP structure [19] is shown in Fig. 2, where the main numerical values which will be of interest for the calculations are indicated. As can be seen in Fig. 2, three regions with different potentials are distinguished in the core/shell tetrapod-shaped nanostructures, *i. e.*, the geometric center or core, the arms and the shell. In this work, the difference between the core and the arms will not be considered, which differ in the crystalline structure of the material, since the tetrapod has been built as the intersection of four cylinders, so the material of the core has the same crystalline structure as the arms. The core region of Fig. 2 has been used in this work to indicate the gap and to establish the reference for the arms and shell potentials.

The Hamiltonian of the problem, within the effective mass approximation, is written in Cartesian coordinates as follows:

$$H = \frac{1}{2m^*_{e,h}}\left(i\hbar\vec{\nabla}_{e,h} \mp e\vec{A}_{e,h}\right)^2 \pm e\,\vec{F}\cdot\vec{r}_{e,h} + V_{e,h}(x,y,z), \tag{1}$$

, where e is the absolute value of the electron charge, $\vec{r} = (x,\ y,\ z)$ stands for the electron position and $m^*_{e,h}$ is the effective mass for electrons (subindex e) and holes (subindex h). The first mathematical sign corresponds to the Hamiltonian for electrons, while the second is associated to the Hamiltonian for the holes. It is important to note that the effective mass will be considered to be position-independent within each of the materials composing the tetrapods.

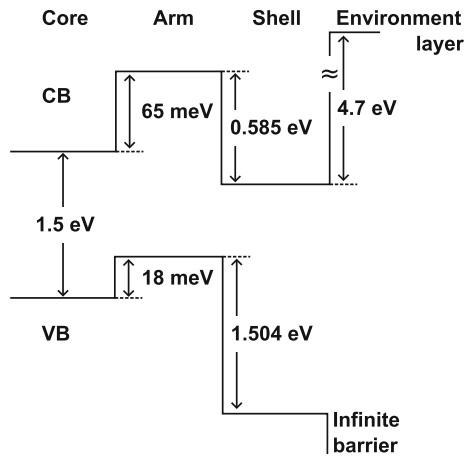

Fig. 2 Confining potential profile corresponding to a CdTe/CdS core/shell tetrapod

The gauge chosen for the description of the magnetic field effect entails the following conditions for the magnetic vector potential of electrons and holes, $\vec{A}$: *(i)* $\vec{\nabla} \cdot \vec{A} = 0$ and *(ii)* $\vec{A} = -\frac{1}{2}\vec{r} \times \vec{B}$. Under the first condition, the Hamiltonian in Eq. 1 takes the form:

$$H = -\frac{\hbar^2}{2m^*_{e,h}}\vec{\nabla}^2_{e,h} \mp \frac{ie\hbar}{m^*_{e,h}}\vec{A}_{e,h} \cdot \vec{\nabla}_{e,h} + \frac{e^2}{2m^*_{e,h}}A^2_{e,h} \pm e\,\vec{F} \cdot \vec{r} + V(x, y, z). \tag{2}$$

In this work, both the electric and magnetic field are applied along the $z-$direction, *i. e.*, $\vec{F} = (F_x,\ F_y,\ F_z) = (0,\ 0,\ F)$ and $\vec{B} = (B_x,\ B_y,\ B_z) = (0,\ 0,\ B)$. From Fig. 1 it is clear that the fields will be parallel to the vertical arm of the tetrapods. Taking into account the second condition mentioned above for the magnetic vector potential, Eq. 2 can be written as:

$$H = -\frac{\hbar^2}{2m^*_{e,h}}\vec{\nabla}^2_{e,h} \mp \frac{ie\hbar}{2m^*_{e,h}}B\left[y\frac{\partial}{\partial x} - x\frac{\partial}{\partial y}\right] + \frac{e^2}{8m^*_{e,h}}B^2\left(x^2 + y^2\right) \pm e\,F\,z + V(x, y, z). \tag{3}$$

The energies and wave functions of the bound states of electrons and holes are obtained with the assumption of parabolic bands as the solutions of the Schrödinger equation:

$$H\,\Psi_i(x, y, z) = E_i\,\Psi_i(x, y, z). \tag{4}$$

Eq. 4 is numerically solved via a finite element method (FEM) as implemented in the COMSOL-Multiphysics software [38]. The Dirichlet boundary condition,$\Psi = 0$, was applied to the outer surface of the GaAs tetrapod, as the wave function must be finite. Similarly, for the core/shell tetrapod: *(i)* wave function continuity on the core-shell interface, $\Psi_{core} = \Psi_{shell}$, *(ii)* BenDaniel-Duke boundary condition: $\frac{1}{m^*_{core}}\frac{\partial\Psi_{core}}{\partial X} = \frac{1}{m^*_{shell}}\frac{\partial\Psi_{shell}}{\partial X}$ with $X = x,\ y,\ z$ and *(iii)* Dirichlet boundary conditions on the outer surface of the CdTe/CdS core/shell tetrapod: $\Psi = 0$.

3 Results and discussion

The Schrödinger equation, shown in Eq. 4, was solved using the FEM via the COMSOL-Multiphysics software [38] within the effective mass approximation. We investigated numerically the lowest confined energy states for electrons and holes in a GaAs tetrapod-shaped nanocrystal and in a CdTe/CdS core/shell tetrapod-shaped nanocrystal subjected to an electric in/or magnetic field as a function of size parameters such as lower radius R_1, upper radius R_2, length of the arm H, shell thickness sh and intensity of the electric and magnetic fields F and B, respectively. The parameters for electrons and holes adopted in numerical calculations are $m^*_{e,\ \mathrm{GaAs}} = 0.067\,m_0$, $m^*_{e,\ \mathrm{CdTe}} = 0.11\,m_0$, $m^*_{e,\ \mathrm{CdS}} = 0.18\,m_0$, $m^*_{h,\ \mathrm{CdTe}} = 0.69\,m_0$, $m^*_{h,\ \mathrm{CdS}} = 0.7\,m_0$ (here, m_0 is the free electron mass) [19, 39] and barrier heights of $V_{core/arm} = 65$ meV and $V_{core/shell} = -0.52$ eV for electrons in CdTe/CdS TP and $V_{core/arm} = -18$ meV and $V_{core/shell} = 1.486$ eV for holes in CdTe/CdS TP, as shown in Fig. 2. The computations were performed for negative and positive values of the electric field F.

For the sake of clarity, this section has been divided in two subsections, the first one is devoted to the analysis of the GaAs tetrapod-shaped nanostructure, while the second one focuses on the CdTe/CdS core/shell tetrapod.

3.1 GaAs Tetrapod

In order to better understand the features of tetrapod-shaped NCs, firstly the single material TP is analyzed. The energies of the first eight electron states are shown in Fig. 3. The first remark that emerges from this figure is that the energies of all states decrease as the

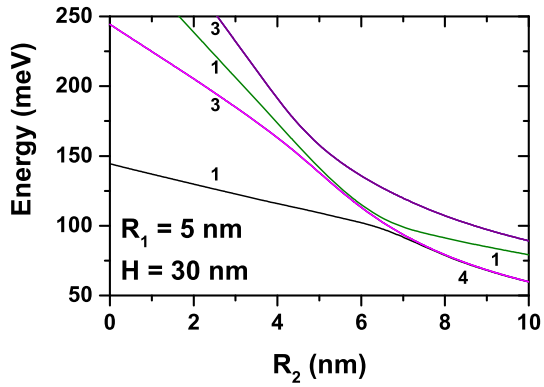

Fig. 3 Variation of the electron energies of the ground and seven first excited states as a function of the upper radius, R_2, for a GaAs tetrapod with fixed lower radius, R_1, and arm length, H. The numbers set by the lines indicate the degeneracy of the energy levels. Calculations correspond to $H = 10$ nm and $R_1 = 5$ nm

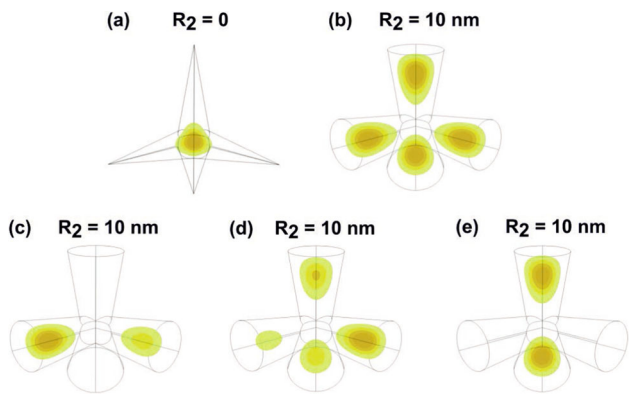

Fig. 4 Squared modulus of the electron wave function in a GaAs tetrapod corresponding to the unique ground state with upper radius $R_2 = 0$ nm (**a**) and the fourfold degenerate ground state with upper radius $R_2 = 10$ nm (**b**) to (**e**). Calculations are for $R_1 = 5$ nm and $H = 30$ nm. Ocher color represents the maximum value, while green is associated to the minimum value

upper radius, R_2, increases. This is a direct consequence of the increment in the volume of the structure originated by the increase in R_2. This feature is in perfect agreement with other studies on nanostructures with different morphologies, such as spherical quantum dots [40, 41]. The numbers set by the lines indicate the degeneracy of the energy levels. Looking at the first four electron states in Fig. 3, a particularity arises from $R_2 \approx 5$ nm. The electron ground state becomes fourfold degenerate given that the electron wave function (EWF) moves from the TP center to the four arms as they shift from a conical morphology for $R_2 = 0$ nm to a cylindrical one as R_2 increases. To clarify this fact, in Fig. 4 the EWF of the ground state is depicted for the two extreme R_2-values considered in this work.

The second step in the analysis of this single material tetrapod-shaped nanostructure is the study of the first eight electron energy states varying simultaneously the length of the four arms, H, maintaining the lower and upper radii equal to each other, $R_1 = R_2 = R = 5$ nm. These results are shown in Fig. 5. The energy of the ground state is well-separated from the first excited states for all values of H, which means that the EWF corresponding to the ground state remains in the geometric center, the core region, as the length of the arms increases. For the sake of clarity, the EWF of the ground state is depicted in panels (a) and (b) of Fig. 6 for the two extreme values of H considered in this study. A close look to the region of larger values of H reveals a tendency for the fourth electron excited state to degenerate with the first three excited states, as their energy gets closer to each other the larger the H-value. As a final remark from Fig. 5, the same trend in the energy behavior already shown in Fig. 3 is found here, given that despite being fixed the cross-section of the arms, their elongation also causes an increase in the volume of the structure. To make clear that the ground state energy also follows this trend, the inset shown in Fig. 5 is a zoomed-in version of this state.

For the sake of completeness, Fig. 7 shows the first electron energy states in the GaAs TP computed for a fixed value of the arm length and varying the arm radii, with the prescription $R_1 = R_2 = R$. As the parameter R moves to larger values, the volume of the structure ascends and, therefore, the energy of all electron states decreases. The latter has been already shown in Figs. 3 and 5. The ground state energy is always well differentiated from the next excited states, indicating that the EWF remains within the core at the geometric center, having an s-like character. To clarify this fact, in Fig. 8 the EWF of the ground state corresponding to the extreme values of R under study are shown in panels (a) and (b), respectively. It is also important to point out the case of the first four excited states. For small values of R, *i. e.*, thin arms, the first excited state is fourfold degenerated given that the EWF is located

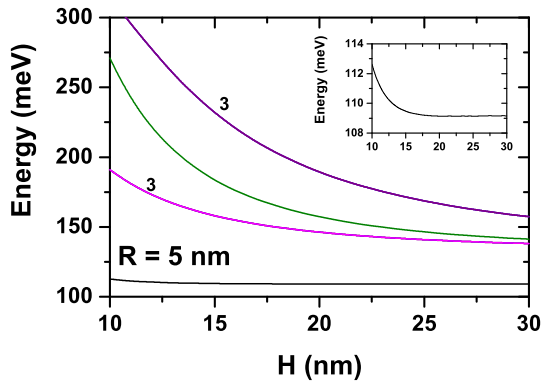

Fig. 5 Variation of the electron energies of the ground and seven first excited states as a function of the arm length, H, for a GaAs tetrapod with fixed lower and upper radii, $R_1 = R_2 = R$. The inset is a zoom for the ground state energy. Numbers set by the lines indicate the degeneracy of the states. Calculations correspond to $R = 5$ nm

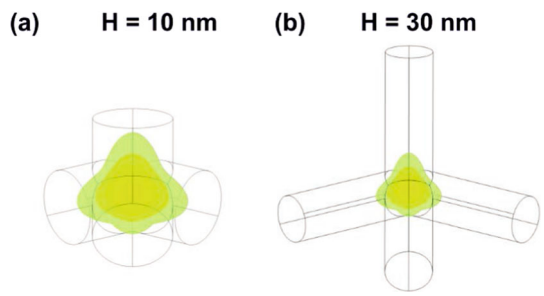

Fig. 6 Squared modulus of the electron wave function corresponding to the ground state in a GaAs tetrapod nanostructure with an arm length of $H = 10$ nm (**a**) and $H = 30$ nm (**b**). Calculations are for equal lower and upper radii, $R_1 = R_2 = R = 5$ nm. Ocher color represents the maximum value, while green is associated to the minimum value

in the four arms of the nanostructure. This behavior has already been shown when analyzing Fig. 5. However, as the radius of the cylinders grow, the state turns to be threefold degenerate, p-like states, as the fourth excited state starts to emerge as a distinguishable energy state at $R \approx 5$ nm, given its s-like symmetry. To clarify, the behavior of the aforementioned fourth excited state, the electron wave function of the first four excited states is shown in panel (b) of Fig. 7. This fourth excited state shows an incipient tendency to degenerate with the next three excited states for larger values of R as can be shown in panel (a) of Fig. 7, the reason to this lying in the fact that the effect of the cylindrical arms is lost for large values of R.

If a GaAs TP with equal lower and upper radii and fixed arm length is now considered, the effect of external electric and magnetic fields is studied. In a first step, the effect of these two fields is studied separately and then, in a second step, their combined effect on the TP nanostructure is analyzed. Figure 9 displays the behavior of the ground state and the first three excited states of the GaAs TP when an external electric field is applied on the nanostructure in the z-axis, both in the positive and negative direction. In the case in which the electric field points to the negative z-axis the EWF is displaced to the vertical TP arm, the energies of the first four electron states are well-separated. As the electric field intensity decreases, the EWF is allowed to move towards the TP core until, for $F = 0$, a threefold degeneracy for the first excited state is found, *i. e.*, the first excited state is a p-like one, which has also been shown in Fig. 7 for $R = 5$ nm. This characteristics are maintained if the electric field is applied along the positive z-direction, up to $F \approx 50$ keV/cm. In all cases, the s-like ground state is deformed to a prolate ellipsoid by the electric field. Given that the electric field affects the $p_{x,y}$-states in the same way, but not the p_z-state, the latter becomes distinguishable from the former two as F increases. For $F > 50$ kV/cm, the EWF is totally pushed towards the lower three TP arms, giving rise to the threefold degenerate ground state that is shown in Fig. 9.

In the absence of an external electric field, the application on the GaAs TP of a magnetic field gives rise to increasing energies for all states, see Fig. 10. The aforementioned impact of the electric field on the s- and $p_{x,y,z}$-states is also valid in the case of the magnetic field, justifying the behavior of the energies of the ground and first three excited states shown in Fig. 10.

When a variable magnetic field and a constant electric field of 150 kV/cm are simultaneously applied on the GaAs TP along the positive z-axis, see Fig. 1, a threefold degenerate ground state is found for all values of the magnetic field, as it is shown in panel (a) of Fig. 11. The reason to this lies on the fact that the electric field pushes the EWF towards the opposite direction. The EWF can, therefore, be located within each one of the three lower arms of the tetrapod with the same probability. As the strength of the magnetic field increases, the energy of the threefold degenerate ground state and the first excited state increase. If the electric field is now applied along the negative z-direction, see panel (b) of Fig. 11, the degeneracy of the ground state is broken, as the EWF

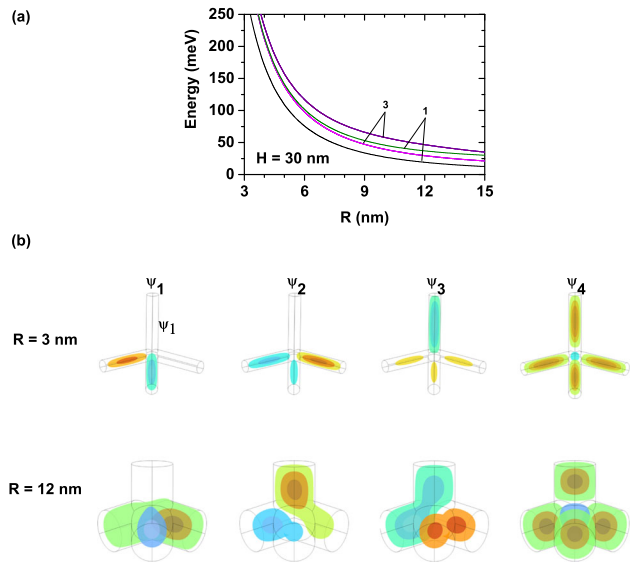

Fig. 7 Electron energy variations corresponding to the ground and seven first excited states as a function of the simultaneous variation of the lower and upper radii, $R_1 = R_2 = R$, for a GaAs tetrapod with fixed arm length, H, **(a)** and electron wave function of the first four excited states, ψ_{1-4}, for two different values of the arm radius **(b)**. Numbers set by the lines in the upper panel indicate the degeneracy of the states. Calculations correspond to $H = 30$ nm. Red color represents the maximum positive value, while blue is associated to the minimum negative value

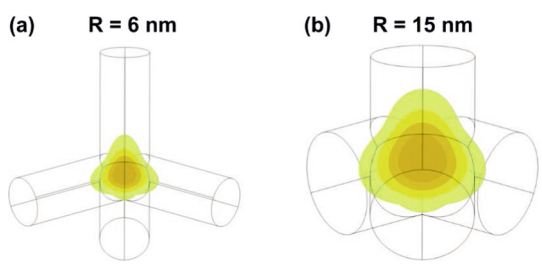

Fig. 8 Squared modulus of the electron wave function corresponding to the ground state in a GaAs tetrapod nanostructure with fixed arm length of $H = 30$ nm and equal lower and upper radii, $R_1 = R_2 = R = 6$ nm (**a**) and $R_1 = R_2 = R = 6$ nm (**b**). Ocher color represents the maximum value, while green is associated to the minimum value

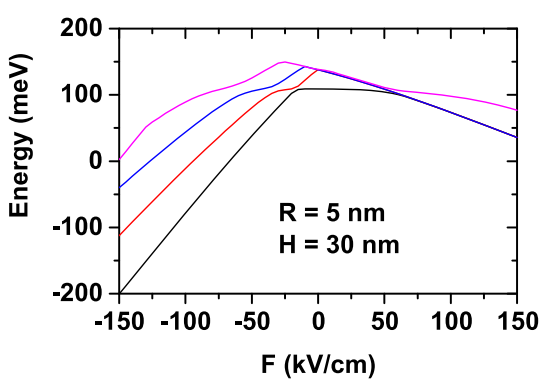

Fig. 9 Electron energy dependence on the externally applied electric field for the ground and first excited states in a GaAs tetrapod with fixed arm length, H and equal lower and upper arm radii, $R_1 = R_2 = R$. Calculations correspond to $H = 30$ nm and $R = 5$ nm

concentrates within the vertical arm of the nanostructure. This justifies also the straight-line-behavior of the energies observed for high magnetic field values.

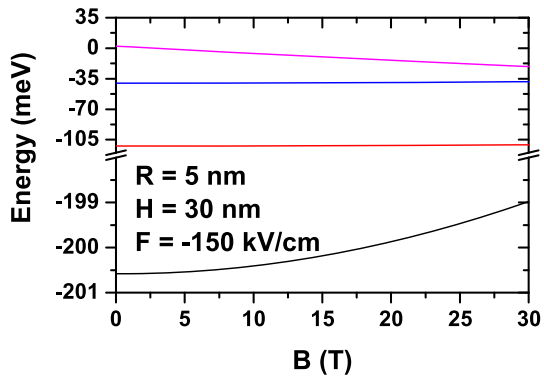

Fig. 10 Electron energy dependence on the externally applied magnetic field for the ground and first excited states in a GaAs tetrapod with fixed arm length, H and equal lower and upper arm radii, $R_1 = R_2 = R$. Calculations correspond to $H = 30$ nm and $R = 5$ nm

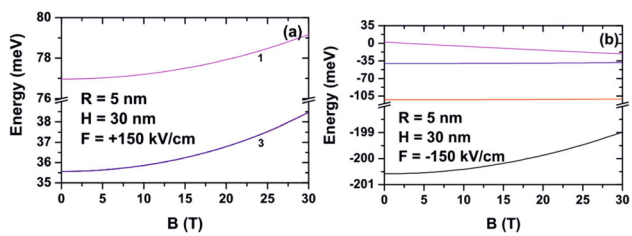

Fig. 11 Electron energy dependence on the externally applied magnetic field for the ground and first excited states in a GaAs tetrapod with fixed arm length, H and equal lower and upper arm radii, $R_1 = R_2 = R$, when a constant electric field of 150 kV/cm is applied on the nanostructure. The magnetic field is directed towards the positive z-direction, while the electric field points to the positive z-direction **(a)** and negative z-direction **(b)**. Numbers by the lines indicate the degeneracy of the states. Calculations correspond to $H = 30$ nm and $R = 5$ nm

3.2 CdTe/CdS core/shell Tetrapod

In order to gain more insight on the physics of the tetrapod-shaped nanostructures, the properties of a CdTe/CdS core/shell TP will be scrutinized along this section. Figure 12 shows the energy dependence on the shell thickness for the first electron and hole states considering two values of the core diameter, see Fig. 1b for notation.

Looking at panels (a) and (b) of Fig. 12, two different regimes are observed, depending on whether the shell thickness, sh, is greater or smaller than ≈ 1.5 nm. Being $sh = 0$ nm the energy gap is of 1.482 eV, as it is straightforward from Fig. 2. In this situation, the system behaves as a type II heterostructure, where the electrons are localized in the core and the holes are confined within the arms. However, once the shell thickness has a non-zero value the energy gap changes to 0.962 eV, see Fig. 2. With this configuration, the electrons tend to localize within the shell, while the holes remain within the arms. The transition between both scenarios for the EWF materializes for $sh \approx 1.5$ nm, as it can be seen in Fig. 12a and b. Once, the EWF is located at the shell, an increase of the shell thickness generates a reduction in the energies, given that the volume of the structure containing the electrons is augmented. The localization of the electrons in each one of the four arms of the TP is equiprobable and, therefore, the electron ground state is fourfold degenerated. Finally, as the holes always remain within the arms of the nanostructure, their energies are essentially independent of the shell thickness, which turns into nearly horizontal lines in panels (c) and (d) of Fig. 12. At this point, it is of paramount importance to note that available experimental data of CdTe/CdS core/shell TPs with $D = 2.2$ nm and $D = 3.7$ nm [19] are in perfect agreement with the numerically calculated data presented in this work.

In order to illustrate the EWF behavior described above, Fig. 13 shows the four isoenergetic electron wave functions associated to the fourfold degenerate ground state in the core/shell TP with $D = 2.2$ nm. It is straightforward from this figure that the EWF tends to displace from the core region to the shell as the shell thickness, sh, becomes increasingly larger.

4 Conclusions

We carried out a theoretical investigation into the energy levels of the first low-lying states for a confined electron in a GaAs and a CdTe/CdS core/shell tetrapod-shaped nanostructure under geometrical modifications and the effect of external electric and magnetic fields. The wave functions and the energy levels were obtained by means of the FEM within the effective mass approximation. For the GaAs TP, the results show that any modification involving an increase in the volume of the tetrapod results in a progressive reduction of the energies of all levels. Particularly interesting is the case of the modification of the upper radius of the arms that, as it increases starting from zero, generates a fourfold degenerated ground state, given that the EWF moves from the core to the four

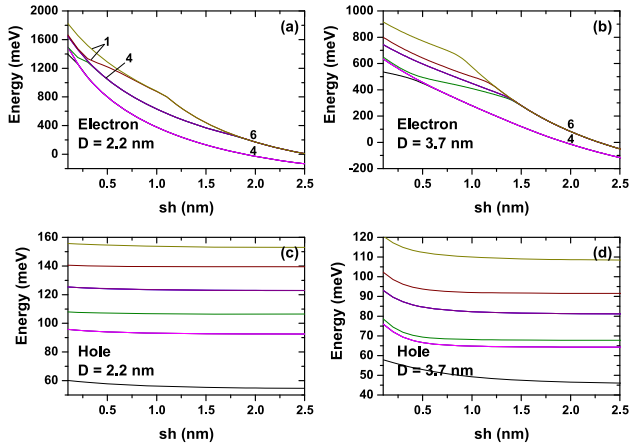

Fig. 12 Energy as a function of the shell thickness, *sh*, for a CdTe/CdS core/shell tetrapod with core diameter $D = 2.2$ nm **(a)**, **(c)** and core diameter $D = 3.7$ nm **(b)**, **(d)**. Upper panels correspond to electron states, while lower panels are represent whole states. Numbers by the electron energies indicate the degeneracy of the states. Calculations correspond to $H = 30$ nm

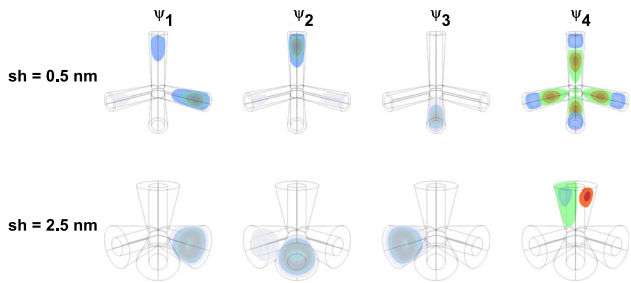

Fig. 13 Illustration of the electron wave functions corresponding to the fourfold degenerate ground state, ψ_{1-4}, for $sh = 0.5$ nm (upper panel) and $sh = 4$ nm (lower panel) in a CdTe/CdS core/shell tetrapod. Calculations correspond to $D = 2.2$ nm and $H = 30$ nm

arms of the nanostructure. When applied separately, the electric and magnetic fields deform the *s*-like EWF of the ground state to a prolate ellipsoid and the displacement of the EWF in the opposite direction of that of the electric field is noticeable. The magnetic field always causes an increase in the energy of all levels. These two effects are also observed under the combined application of the electric and magnetic fields. Finally, the variation of the energies of the first electron and hole states in the CdTe/CdS core/shell TP was analyzed as a function of the shell thickness for two different core diameters. The results suggest the existence of two different regimes based on the band alignment of the core, the arms and the shell, once the latter has a relevant thickness. The transition between both regimes occurs at a thickness of ≈ 1.5 nm and is characterized by the shifting of the EWF from the core to the shell, while the wave function of the holes remains in the arms at all cases. Our calculated results thoroughly reproduce the experimental results already published for this tetrapod-shaped nanostructure with the same dimensions and material specified here. The analysis of core/shell TPs subjected to external electric and magnetic fields, as well as of the electronic and optical properties of GaAs and CdTe/CdS core/shell TPs with impurities are under further investigation and will be published elsewhere.

Acknowledgements R.V.H.H. gratefully acknowledges financial support from the Spanish Junta de Andalucía through a Doctoral Training Grant. The authors are grateful to Colombian agencies CODI-Universidad de Antioquia (Estrategia de Sostenibilidad de la Universidad de Antioquia and projects "Propiedades magneto-ópticas y óptica no lineal en superredes de Grafeno", "Estudio de propiedades ópticas en sistemas semiconductores de dimensiones nanoscópicas", "Propiedades de transporte, espintrónicas y térmicas en el sistema molecular ZincPorfirina", "Complejos excitónicos y propiedades de transporte en sistemas nanométricos de semiconductores con simetría axial", and "Nanoestructuras semiconductoras con simetría axial basadas en InAs y GaAs para aplicaciones en electrónica ultra e híper rápida") and Facultad de Ciencias Exactas y Naturales-Universidad de Antioquia (A.L.M. and C.A.D. exclusive dedication projects 2023–2024). R.L. Restrepo would like to thank the Universidad EIA, Colombia, throught the research project "Simulación por el método de elementos finitos de las respuestas ópticas de nanoestructuras semiconductoras aplicadas en imágenes médicas" (Código: INVIM0442023). J.A.V. acknowledges to the Institución Universitaria-ITM.

Author Contributions The contributions of the authors are as follows: R.V.H. H. worked on the analysis of the results, discussions, writing of the preliminary manuscript and revision of the final version. F.M.R. and J.M.S. and J.A.V.: worked on numerical computations, programming codes, and outcomes analysis. R.L.R. and G.E. and M.G.B. and A.E.D. and D.A.D.: worked on the formal analysis and writing of the manuscript. A.L.M. and C.A.D.: proposed the problem and worked on the numerical calculations and writing of the manuscript.

Funding Open Access funding provided by Colombia Consortium.

Data Availability Statement The manuscript has associated data in a data repository. [Author's comment: All the files with tables, figures, and codes are available. The corresponding author will provide all the files in case they are requested.]

Declarations

Conflict of interest The authors do not have any financial and non-financial competing interests statement.

Open Access This article is licensed under a Creative Commons Attribution 4.0 International License, which permits use, sharing, adaptation, distribution and reproduction in any medium or format, as long as you give appropriate credit to the original author(s) and the source, provide a link to the Creative Commons licence, and indicate if changes were made. The images or other third party material in this article are included in the article's Creative Commons licence, unless indicated otherwise in a credit line to the material. If material is not included in the article's Creative Commons licence and your intended use is not permitted by statutory regulation or exceeds the permitted use, you will need to obtain permission directly from the copyright holder. To view a copy of this licence, visit http://creativecommons.org/licenses/by/4.0/.

References

1. P.K. Chattopadhyay, D.A. Price, T.F. Harper, M.R. Betts, J. Yu, E. Gostick, S.P. Perfetto, P. Goepfert, R.A. Koup, S.C. De Rosa et al., Nat. Med. **12**, 972 (2006)
2. J. Kolosnjaj-Tabi, Y. Javed, L. Lartigue, J. Volatron, D. Elgrabli, I. Marangon, G. Pugliese, B. Caron, A. Figuerola, N. Luciani et al., ACS Nano **9**, 7925 (2015)
3. D.V. Talapin, J.-S. Lee, M.V. Kovalenko, E.V. Shevchenko, Chem. Rev. **110**, 389 (2010)
4. I. Kriegel, C. Jiang, J. Rodríguez-Fernández, R.D. Schaller, D.V. Talapin, E. da Como, J. Feldmann, J. Am. Chem. Soc. **134**, 1583 (2012)
5. S. Kim, S. Park, M. Kim, S. Jeong, Bull. Korean Chem. Soc. **44**, 483 (2023)
6. H. Lee, D.-E. Yoon, S. Koh, M.S. Kang, J. Lim, D.C. Lee, Chem. Sci. **11**, 2318 (2020)
7. F. Huang, J. Ning, Z. Duan, A.A. Sergeev, A. Portniagin, S.V. Kershaw, J. Tian, A.L. Rogach, Chem. Mater. **33**, 2398 (2021)
8. N. Mishra, V. G. Vasavi Dutt, M. P. Arciniegas, Chemistry of Materials **31**, 9216 (2019)
9. Z. Liu, R. Pascazio, L. Goldoni, D. Maggioni, D. Zhu, Y.P. Ivanov, G. Divitini, J.L. Camarelles, H.B. Jalali, I. Infante et al., J. Am. Chem. Soc. **145**, 18329 (2023)
10. M.J. Enright, F.Y. Dou, S. Wu, E.J. Rabe, M. Monahan, M.R. Friedfeld, C.W. Schlenker, B.M. Cossairt, Chem. Mater. **32**, 4774 (2020)
11. B. Kim, K. Kim, Y. Kwon, W. Lee, W.H. Shin, S. Kim, J. Bang, ACS Appl. Nano Mater. **1**, 2449 (2018)
12. W.-Y. Wu, M. Li, J. Lian, X. Wu, E.K.L. Yeow, M.H. Jhon, Y. Chan, ACS Nano **8**, 9349 (2014)
13. R. Zhao, Y. Liu, C. Liu, G. Xu, Y. Chen, Y. Tang, T. Lu, J. Mater. Chem. A **2**, 20855 (2014)
14. T. Mokari, E. Rothenberg, I. Popov, R. Costi, U. Banin, Science **304**, 1787 (2004)
15. M. Samadi Khoshkhoo, P. Zhang, K. Hiekel, B. Martín-García, A. Reichhelm, V. Lesnyak, A. Eychmüller, Chem. Mater. **32**, 4045 (2020)
16. Y. Khalavka, C. Sönnichsen, Adv. Mater. **20**, 588 (2008)
17. S. Kim, B. Fisher, H.-J. Eisler, M. Bawendi, J. Am. Chem. Soc. **125**, 11466 (2003)
18. S. Kumar, M. Jones, S.S. Lo, G.D. Scholes, Small **3**, 1633 (2007)
19. Y. Yao, T. Kuroda, D.N. Dirin, M.S. Sokolikova, R.B. Vasiliev, Superlatt. Microstruct. **76**, 244 (2014)
20. H. Zhong, Y. Zhou, Y. Yang, C. Yang, Y. Li, J. Phys. Chem. C **111**, 6538 (2007)
21. B. Sun, E. Marx, N.C. Greenham, Nano Lett. **3**, 961 (2003)
22. D. Zhao, Z. He, W.H. Chan, M.M.F. Choi, J. Phys. Chem. C **113**, 1293 (2009)
23. D.N. Dirin, R.B. Vasiliev, M.S. Sokolikova, A.M. Gaskov, Inorg. Mater. **47**, 23 (2011)
24. M. Califano, Y. Zhou, ACS Appl. Nano Mater. **5**, 18986 (2022)
25. S. Koh, H. Lee, J. Y. Woo, W. Ki Bae, Y.-S. Park, D. C. Lee, J. Phys. Chem. C **126**, 17176 (2022)
26. J. Llusar, I. Infante, et al., in *Proceedings of MATSUS23 & Sustainable Technology Forum València (STECH23)(MATSUS23)* (2022)
27. X. Wang, S. Chen, S. Thota, Y. Wang, H. Tan, M. Tang, Z. Quan, J. Zhao, J. Phys. Chem. C **123**, 19238 (2019)
28. D.V. Talapin, J.H. Nelson, E.V. Shevchenko, S. Aloni, B. Sadtler, A.P. Alivisatos, Nano Lett. **7**, 2951 (2007)
29. C. Mauser, T. Limmer, E. Da Como, K. Becker, A.L. Rogach, J. Feldmann, D.V. Talapin, Phys. Rev. B **77**, 153303 (2008)
30. L. Yan, A. Uddin, H. Wang, Nanomater. Nanotechnol. **5**, 19 (2015)
31. J. Yang, Z. Zhang, Y. Qin, ACS Appl. Mater. Interfaces **8**, 22392 (2016)
32. H. Lee, S. Yoon, J. Ahn, Y. Suh, J. Lee, H. Lim, D. Kim, Sol. Energy Mater. Sol. Cells **93**, 779 (2009)
33. N. Mishra, W.-Y. Wu, B.M. Srinivasan, R. Hariharaputran, Y.-W. Zhang, Y. Chan, Chem. Mater. **28**, 1187 (2016)
34. S.N. Raja, D. Zherebetskyy, S. Wu, P. Ercius, A. Powers, A.C.K. Olson, D.X. Du, L. Lin, S. Govindjee, L.-W. Wang et al., Nano Lett. **16**, 5060 (2016)
35. Y. Liao, G. Xing, N. Mishra, T. C. Sum, Y. Chan, Adv. Mater. **24**, OP159 (2012)
36. Y. Cui, U. Banin, M.T. Björk, A.P. Alivisatos, Nano Lett. **5**, 1519 (2005)
37. M. Zavelani-Rossi, M.G. Lupo, R. Krahne, L. Manna, G. Lanzani, Nanoscale **2**, 931 (2010)
38. C. Multiphysics, COMSOL Multiphysics, Burlington, MA, accessed Feb **9**, 2018 (1998)
39. W. Nakwaski, Physica B **210**, 1 (1995)
40. S. Kumar, M. Nehra, A. Deep, D. Kedia, N. Dilbaghi, K.-H. Kim, Renew. Sustain. Energy Rev. **73**, 821 (2017)
41. S. Kabi, A.G.U. Perera, J. Appl. Phys. **117**, 124303 (2015)